*Conference Paper*

# Horizontal Axis Wind Turbine Aerodynamics: Three-Dimensional, Unsteady, and Separated Flow Influences

M.C. Robinson, M.M. Hand, D.A. Simms, S.J. Schreck

**NREL**

**National Renewable Energy Laboratory**

**NOTICE**

# FEDSM99-S295-01

# HORIZONTAL AXIS WIND TURBINE AERODYNAMICS:
## THREE-DIMENSIONAL, UNSTEADY, AND SEPARATED FLOW INFLUENCES

M. C. Robinson
National Renewable Energy Laboratory
1617 Cole Blvd., Golden, CO 80401
Michael.Robinson@nrel.gov

D. A. Simms
National Renewable Energy Laboratory
1617 Cole Blvd., Golden, CO 80401
David_Simms@nrel.gov

M. M. Hand
National Renewable Energy Laboratory
1617 Cole Blvd., Golden, CO 80401
Maureen_Hand@nrel.gov

S. J. Schreck
National Renewable Energy Laboratory
1617 Cole Blvd., Golden, CO 80401
Scott_Schreck@nrel.gov

**ABSTRACT**

Surface pressure data from the National Renewable Energy Laboratory's "Unsteady Aerodynamics Experiment" were analyzed to characterize the impact of three-dimensionality, unsteadiness, and flow separation effects observed to occur on downwind horizontal axis wind turbines (HAWT). Surface pressure and strain gage data were collected from two rectangular planform blades with S809 airfoil cross-sections, one flat and one twisted. Both blades were characterized by the maximum leading edge suction pressure and by the azimuth, velocity, and yaw at which it occurred. The occurrence of dynamic stall at all but the inboard station (30% span) shows good quantitative agreement with the theoretical limits on inflow velocity and yaw that should yield dynamic stall events. A full three-dimensional characterization of the surface pressure topographies combined with flow visualization data from surface mounted tufts offer key insights into the three-dimensional processes involved in the unsteady separation process and may help to explain the discrepancies observed with force measurements at 30% span. The results suggest that quasi-static separation and dynamic stall analysis methods relying on purely two-dimensional flow characterizations may not be capable of simulating the complex three-dimensional flows observed with these data.

**INTRODUCTION**

Wind turbine aerodynamic loads routinely exhibit startling spatial and temporal complexities, driven by the combined influences of three-dimensionality, unsteadiness, and dynamic separation. Three-dimensional cross flows as well as quasi-steady and unsteady separation events arise from both the stochastic nature of the inflow and the components of the turbine architecture. Rapid changes in wind speed or direction dynamically alter the local angle of attack along the span. Both angle of attack and dynamic pressure change radially along the span, and are further effected by variable speed or pitch operation. Because of these many influences, accurate and reliable prediction of wind turbine aerodynamics remains a unique challenge for today's computational modelers.

The overall contribution of dynamic stall to wind turbine structural loads continues to undergo opinion shifts in the research community. Several years ago, the effects of dynamic stall were deemed inconsequential as interest centered around predicting power performance. This conclusion was not surprising since the rapid transient loads produced by a single dynamic stall event occur over a small percentage of the total turbine rotation cycle. Opinions changed when it was shown that some type of dynamic stall model was necessary to adequately predict both peak and fatigue loads. Currently, the impulsive loading introduced via dynamic stall aerodynamic models can be shown to amplify, damp, or have little effect on the resulting structural loads depending on a particular time series, turbulent inflow condition, or turbine architecture.

As such, the ability of current aerodynamic models to adequately predict quasi-steady, three-dimensional, post-stall performance remains in question, let alone three-dimensional dynamic stall performance in an extremely stochastic inflow environment. Most wind turbine structural design codes rely on Blade Element Momentum Theory (BEMT) to simulate blade aerodynamic performance. This algorithm allows the aerodynamics model to run quickly, enabling practical design trade-off analyses. The use of empirical two-dimensional wind

tunnel test data to obtain quasi-static aerodynamic loads and necessary assumptions associated with BEMT prevents these models from capturing full three-dimensional effects. These aerodynamics models include dynamic stall models, again empirically derived using two-dimensional wind tunnel test data collected from pitching and plunging type motions. Further refinements can be made for three-dimensional tip and separation effects. It is not clear, however, if the resulting integrated aerodynamics models sufficiently capture the actual fluid physics of highly three-dimensional, dynamically separated flows in the presence of stochastic inflows. Nor is it clear to what degree these models are able to produce adequate predictions experienced in the full operating envelope of a field environment.

Data from the Unsteady Aerodynamics Experiment are often used for validation of aerodynamic design models. In fact, some 400 authors have cited use of the Unsteady Aerodynamics Experiment data set including 26 papers this year alone. Much of the data are readily available over the internet through collaborative IEA interactions [1]. The most widely used data sets represent "baseline" conditions. Under these conditions, wind speed and yaw error do not undergo extreme variations during multiple successive rotation cycles, and approximate steady, deterministic inflow conditions as closely as possible. These "baseline" data comprise less than 3% of all cycles collected, providing a clear indication of the highly stochastic nature of actual field operation.

Unfortunately, only successful model validation comparisons are likely to be published in the open literature. However, model predictions that agree closely with field test data correspond to relatively benign operating conditions. In general, model predictions fail to agree well with Unsteady Aerodynamics Experiment data, where separation and strong three-dimensional effects dominate the blade/inflow interaction. Most analysts and designers agree that aerodynamic model predictions in such flow regimes are suspect, and should be used only with appropriate safety factors based on design and field experience.

It is also uncertain that sufficiently detailed field measurements exist for validating aerodynamics models against the actual three-dimensional, unsteady fluid physics. Attempting to glean aerodynamic performance data from experimental field data is an extremely difficult task. Stochastic inflow conditions vary three-dimensionally with spatial scales less than the characteristic rotor diameter. Measuring a simple performance parameter, like instantaneous angle of attack at a specific span location, becomes extremely difficult in a time varying, three-dimensional field test environment. Further, one must be cognizant of wake effects in that the data obtained in any single rotation cycle serves as an integrated result of several previous rotations. Capturing the characteristics and nuances of three-dimensional flow separation in a stochastic inflow environment on a large piece of rotating machinery poses as significant a challenge as understanding the underlying fluid physics.

The following Unsteady Aerodynamics Experiment data compare the performance characteristics of two different experimental rotors tested at the National Wind Technology Center. This comparison utilizes the entire data set from both rotors, providing a global performance overview across all observed wind speeds and yaw errors. Data represent means and standard deviations computed for individual cycles. These data have been binned according to cycle averaged wind speed and yaw error. Where interesting anomalies occur in the cycle averaged data, time series data also are presented to emphasize differences between cycle averages and single cycle transient events. Highlighted are the three-dimensional effects of blade twist and resulting aerodynamic performance in attached, stalled, and yawed flow. These results provide some insight into turbine operation under normal field operation, where unsteady, separated, and strongly three-dimensional flow responses are common events.

.

## NOMENCLATURE

| | | |
|---|---|---|
| $\alpha$ | angle of attack | |
| $\phi$ | blade azimuth angle | |
| $\varphi$ | yaw error | |
| $\rho$ | density | |
| c | chord | |
| q | dynamic pressure | $\{1/2\rho V^2)\}$ |
| p | static pressure | |
| M | blade moment | |
| N' | normal force per unit span | |
| r | span location | |
| R | blade span length | |
| S | blade planform area | |
| V | velocity | |
| $C_M$ | flap bending moment coefficient | $\{M/(q_T SR)\}$ |
| $C_N$ | normal force coefficient | $\{N'/(qc)\}$ |
| $C_p$ | pressure coefficient | $\{(p-p_\infty)/q\}$ |
| i | local span conditions | |
| $\infty$ | free stream conditions | |
| T | blade tip conditions | |

## UNSTEADY AERODYNAMICS FIELD EXPERIMENT

The Unsteady Aerodynamics Experiment horizontal axis wind turbine (Fig. 1) is well documented [2-5]. The 10.1m diameter, three-bladed downwind machine rotates at a constant 72 rpm and is capable of producing 20 kW of power. A cylindrical tower 0.4 m in diameter supports the turbine at a hub height of 17 m. This generic configuration has been used for five different phases of the experiment. The test configuration for each phase and data collected are summarized in Table 1.

**Table I:** Summary of test configurations.

|  | Phase II | Phase III | Phase IV | Phase V |
|---|---|---|---|---|
| Configuration | 3-blade, Constant Chord, Untwisted | 3-blade, Constant Chord, Twisted | 3-blade, Constant Chord, Twisted | 2-blade, Constant Chord, Twisted |
| Total10-minute Campaigns | 29 | 19 | 75 | 74 |
| Non-Rotating Campaigns |  | 2 minutes | 9 90 minutes | 11 110 minutes |
| -9° Pitch Angle |  |  | 1 720 cycles | 6 4320 cycles |
| -3° Pitch Angle |  |  | 12 8640 cycles | 11 7920 cycles |
| 3° Pitch Angle |  | 19 13,680 cycles | 39 28,080 cycles | 37 26,660 cycles |
| 8° Pitch Angle |  |  | 12 8,640 cycles | 6 4320 cycles |
| 12° Pitch Angle | 29 20,880 cycles |  | 1 720 cycles | 1 720 cycles |
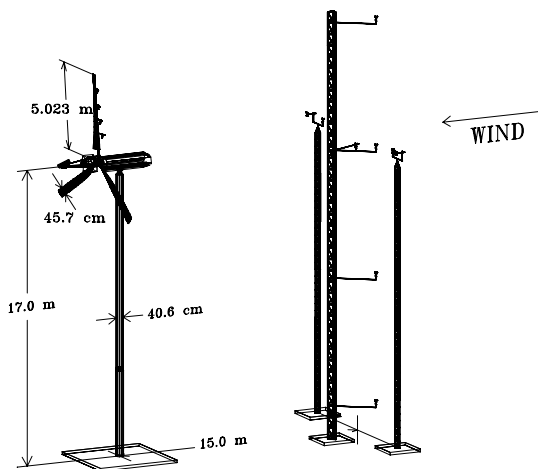


**Figure 1:** Combined experiment isometric.

Data from Phase II and Phase IV were used for the comparisons documented herein. Both the Phase II and Phase IV rotors had three blades of 5.04 m radius. All blades were of rectangular planform, and used NREL S809 airfoil cross-sections with a 0.457 m chord. Phase II rotor blades were untwisted, while Phase IV blades had twist distributions optimized to yield a uniform 15° angle of attack at a wind speed of 8 m/s. One blade on each rotor was thoroughly instrumented with pressure transducers (Fig. 2). Phase II employed four instrumented span locations (30%, 47%, 63%, and 80% span). Phase IV added an instrumented span location at 95% span. Dynamic pressure and inflow angle were also measured at or near these four span locations. The data sample rate (521 Hz) was sufficient to capture dynamic and transient pressure events elicited from time varying inflow conditions. Wind magnitude and direction were measured 12-15 m upwind of the turbine using cup, propeller, and sonic anemometers.
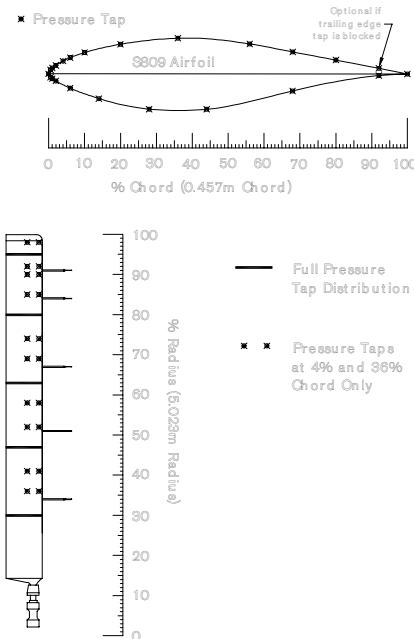


**Figure 2:** Blade pressure tap locations

It is important to note that both the rectangular and twisted blade geometries used for the Unsteady Aerodynamics Experiment are atypical. Multiple Unsteady Aerodynamics Experiment program phases were designed to provide a common data set for comparing three-dimensional blade geometry effects on aerodynamic performance. Hence, the blade geometry has been altered parametrically, and all other variables have been held as constant as physical design constraints would allow. The blade that will be tested next in the Unsteady Aerodynamics Experiment program will be an optimized tapered and twisted blade. This blade was designed in accordance with current "best practice" standards and is typical of blades used by industry. This blade will be tested in both a field (NWTC) and wind tunnel (NASA Ames 80ft x 120ft) environment, providing a comprehensive data set for developing and validating new aerodynamics codes.

## ANGLE OF ATTACK SENSITIVITY TO INFLOW AND TURBINE GEOMETRY

To fully appreciate the three-dimensional aerodynamic response of turbine rotors, it is important to consider the interrelated effects of blade geometry, pitch, and rotation rate, as well as turbine architecture, wind magnitude and direction on the local angle of attack ($\alpha$). Local blade angle of attack is a function of the vector sum of the local inflow and rotor angular velocity. Small variations drive the local blade angle of attack beyond the S809 static stall angle of 15.2°. Blade rotation decreases $\alpha$ at span locations closer to the tip. Thus, inboard span locations experience larger variations in $\alpha$ for any given inflow condition. Downwind turbines, like the Unsteady

Aerodynamics Experiment, experience an additional complexity. Tower shadow occurs when the wake from the cylindrical tower intersects the rotor plane down stream. As the blade rotates into the tower shadow ($\phi \approx 180°$, depending on yaw error), the wake velocity deficit first decreases $\alpha$ until it reaches a minimum at the tower wake center. Then, $\alpha$ rapidly increases as the blade moves out of the wake. The presence of the tower shadow is additive to the other variables effecting $\alpha$ and will be shown to have a predominant effect on the overall aerodynamic performance data reported below.

The wake behind the cylindrical tower support is inherently unsteady, being dominated by vortex shedding. In addition, the local tower Reynolds number can transition between sub-critical and critical ranges in response to routine changes in wind speed. The resulting variation in blade $\alpha$ through the tower shadow region is correspondingly unsteady and complex. Empirical models normally rely on time averaged velocity deficit wake models producing quasi-static $\alpha$ changes through the tower wake. Unsteady Aerodynamics Experiment data [6] have shown tower wake flow to be strongly vortical. Given the time varying vortical flow in the tower wake, even with all other parameters remaining constant, it is unlikely that two subsequent blade rotation cycles through the tower wake would produce the same transient aerodynamic response. These authors are unaware of detailed rotating blade/wake interaction investigations that have quantified this effect in sufficient detail to support comprehensive model validation.

These blade/inflow/tower wake interactions can elicit substantial dynamic alterations in $\alpha$, generating appreciable transient aerodynamic responses. Under certain conditions, $\alpha$ variations are sufficient to produce dynamic stall over portions of the rotating blade. The readers are referred to extensive reviews of dynamic stall from unsteady pitching and plunging lifting surfaces [7,8]. For horizontal wind turbines operating at high tip speed ratios, rapid inflow changes create the same dynamic $\alpha$ variation and transient aerodynamic response. However, dynamic stall is only one of several effects in the near and post-stall operating environment producing transient effects. Both three-dimensional quasi-static and unsteady effects from tower shadow and the stochastic inflow will be shown to play a role as significant as dynamic stall on the transient loads.

The complex interrelationships between $\alpha$ variation, turbine geometry, and inflow are shown in Fig. 3 for the Phase IV (twisted blade) rotor. The three plots show the variation in local angle ($\alpha$) over the blade span with blade rotation through a full cycle ($\phi = 0°$ to $360°$). The three plots top to bottom correspond to yaw errors ($\varphi$) of $+20°$, $0°$, and $-20°$ at a single uniform inflow velocity ($V_\infty = 20$ m/sec). All of the data were generated using YawDyn, and include a turbine wake model and tower shadow effect. Local angle ($\alpha$) is extremely sensitive to the axial induction factor as well as to the other parameters noted earlier. Very different results can be produced with different models, and the principal intent is to demonstrate the

three-dimensional variability along the span. In fact, when inflow turbulence is added, effecting both inflow magnitude and direction, these relationships become much more complex. One notable effect that also will be seen in the experimental data, is the phase relationship between the tower shadow and $\alpha$ variation due to $\varphi$.
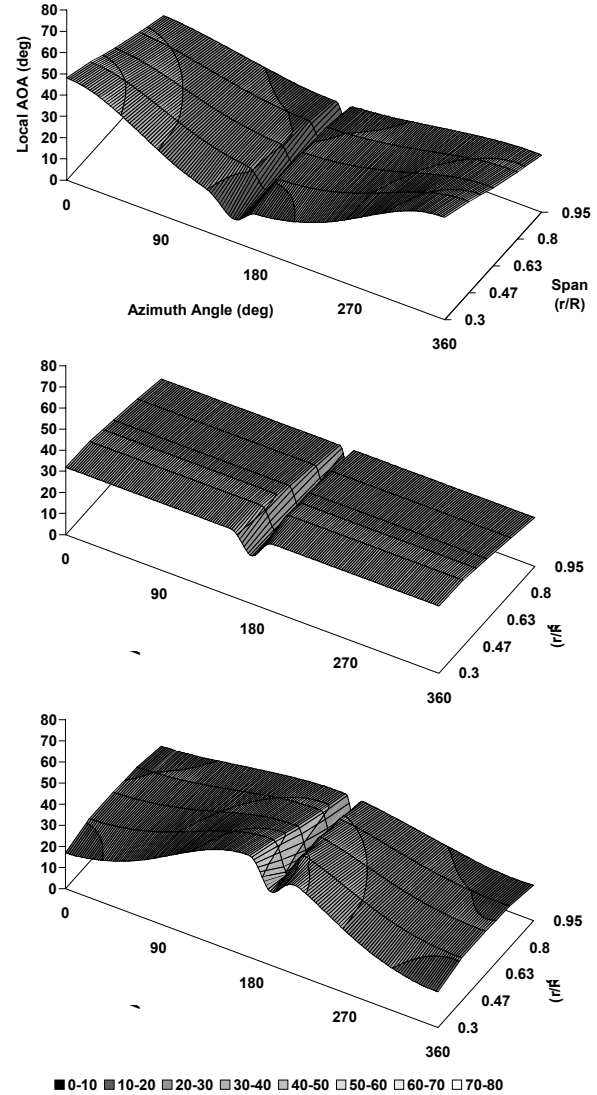


**Figure 3:** Local angle of attack ($\alpha_i$) cyclic variation with blade azimuth angle ($\phi$), span ($r_i$), yaw error ($\varphi$). Yaw errors of $20°$ (upper panel), $0°$ (middle panel), and $-20°$ (lower panel).

## DATA DENSITY AND INFLOW CONDITIONS

The Unsteady Aerodynamics Experiment turbine is a three-bladed, downwind, free yaw machine. Of all the data collected for the two geometries (Table 1), the largest data sets are for pitch angles of $12°$ and $3°$ for the untwisted (Phase II) and twisted (Phase IV) geometries, respectively. The data

densities for Phase IV are presented graphically as the number of cycles binned according to cycle mean values of wind speed and yaw error in Fig. 4. Bin dimensions are 2.0 m/s for wind speed and 5° for yaw error. In the upper plot, the entire Phase IV data set corresponding to a 12° pitch angle is included and plotted using a contour increment of 100 cycles. In the lower plot, to better resolve data distribution at the extremes of $V_\infty$ and $\varphi$, bins containing 100 or more cycles were omitted, and the remaining bins were contour plotted with a contour interval of 10 cycles. During field tests, engineers had noted the propensity for the turbine to remain at slightly negative $\varphi$'s under steady winds. Consistent with these observations, the upper plot in Fig. 4 shows that, between 6 and 17 m/s, $\varphi$ most frequently assumed a value between -5° and -10°.
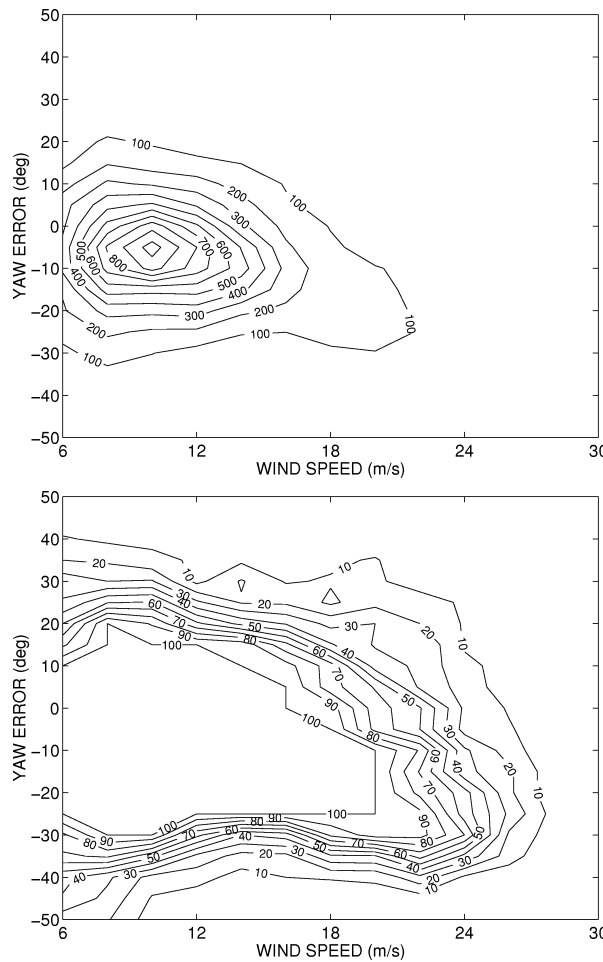


**Figure 4:** Number of cycles as a function of mean velocity ($V_\infty$) and yaw error ($\varphi$).

Fig. 5 contains inflow turbulence intensity plotted for all cycles in two different ways. First, standard deviations were computed for 10 minute data records and binned according to the 10 minute mean velocity (identified in the legend as "10-min."). Second, standard deviations were computed for each cycle and binned according to the cycle average velocity (all traces not identified as "10-min."). The 10-minute average data show the typical decrease in turbulence intensity with increasing wind speed. Clearly, insufficient numbers of 10-minute data sets are available to allow statistically significant comparisons, but the trends are evident. The low deviations for the single cycle statistics are much more germane to the current analysis. For literally thousands of cycles, standard deviations for $V_\infty$ are less than 5% for mean velocities between 5 m/s and 25 m/s. As one would expect, the sonic anemometers show higher deviations than the cup or propeller instruments due to bandwidth. Standard deviations significantly exceed 5% below 5 m/s mean velocity and above 25 m/s. At low mean velocities, this is due to division by low mean velocities. At high mean velocities, this is caused by the tendency of sonic anemometers to give false readings from dust and debris.
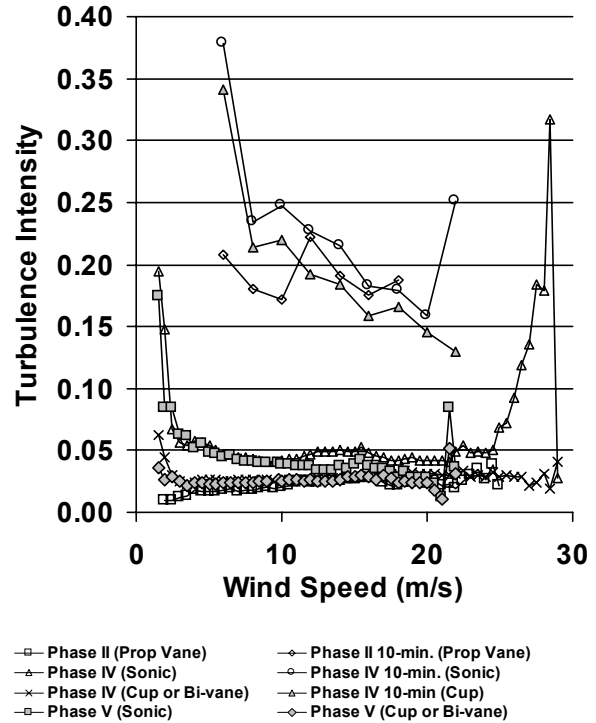


**Figure 5:** Turbulence intensity versus average wind speed.

The same format and trends are apparent in $\varphi$ (Fig. 6). Yaw error data collected from mechanical bi-vanes are in excellent agreement with the values for $\varphi$ calculated from the sonic anemometer. For the single cycle statistics, yaw error standard deviations are less than 5% for all mean wind speeds between 7 m/s and 25 m/s. Thus, binning aerodynamic performance on cycle mean averaged $V_\infty$ and $\varphi$ provide a

5

reasonable global overview of blade performance across a wide range of parametric changes.
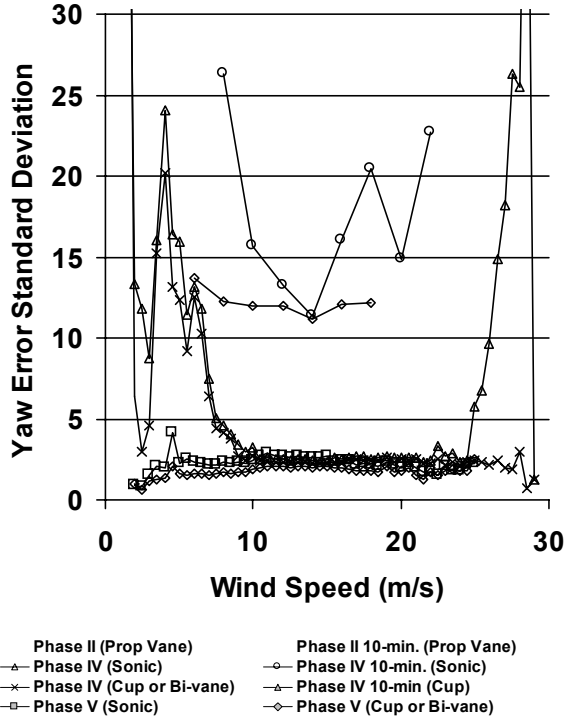


**Figure 6:** Yaw error standard deviation versus average wind speed.

## COMPARISON WITH TWO-DIMENSIONAL RESULTS

Normal force coefficients ($C_N$) for both blades and all span locations are shown as a function of local $\alpha$ in Fig. 7. There is excellent agreement with two-dimensional wind tunnel data at $\alpha$'s lower than static stall ($\alpha$=15.2°). Above stall, data corresponding to 30% span show the most radical departure, with $C_N$ values reaching values of nearly 3.0. For comparison, $C_p$ on the suction surface of an S809 at a Reynolds number of 500,000 never decreases below a value of -5.0. The peak $C_N$ occurs at approximately 0.9 [2]. At a Reynolds number of 2,000,000, the peak $C_N$ increases to 1.1, again with $C_p$ minima remaining above -5.0 [9].

Notably, in near and post-stall flow, $C_N$ values for all span locations greatly exceed two-dimensional wind tunnel data. Associated $C_p$ minima decrease substantially below static minima, as documented below. Visualization using fine thread tufts fixed to the upper blade surface shows attached and two-dimensional flow until the onset of stall. As separation initiates at the trailing edge and propagates forward with increasing $\alpha$, flow over the upper surface becomes immediately three-dimensional, with flow in the separated region moving toward the blade tip. This three-dimensional flow, once established, appears very stable in the visualizations with tufts over the aft

portion of the chord pointing radially toward the tip with little deviation.

If the inflow direction produces significant yaw error, or if the inflow magnitude creates a local angle of attack near stall, the resulting flow effect can be extremely dynamic. Cyclic three-dimensional unsteady separation and reattachment from both tower shadow and yawed inflow can occur within a single rotation cycle. This three-dimensional separation in near-stall and post-stall flow conditions is responsible for the large aerodynamic loads that exceed static stall values.
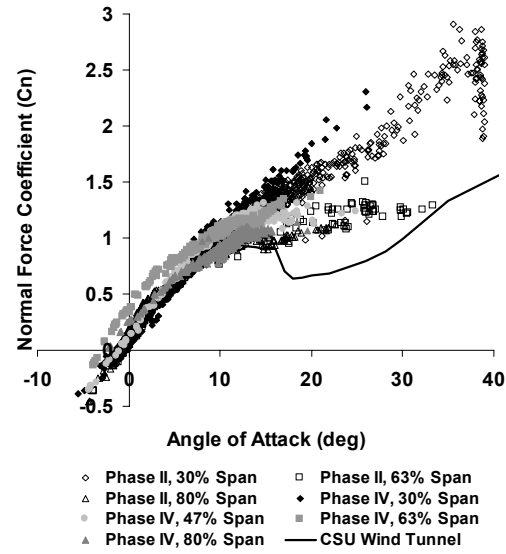


**Figure 7:** $C_N$ versus $\alpha_i$ for baseline conditions.

## THREE-DIMENSIONAL PERFORMANCE EFFECTS

Pressure coefficient ($C_p$) variation over a rotation cycle was used to provide a metric of the increased blade loading due to three-dimensional dynamic response. For each span location, all data cycles were binned on cycle mean averaged $V_\infty$ and $\varphi$. If the pressure coefficient decreased below a threshold value of $C_p = -8.0$, the cycle was recorded. Fig. 8 shows the percentage of cycles meeting this criterion over the range of $V_\infty$ and $\varphi$, for the twisted blade. In this figure, only the 30% and 80% span locations are shown. On each figure, the left boundary indicates the conditions for $V_\infty$ and $\varphi$ where the static stall angle is reached as a maximum during the rotation cycle ($\alpha = 15.2°$). The right boundary demarcates where the static stall angle is reached as a minimum during the cycle. At both span locations, the most prominent contour features lie between these two boundaries. Hence, the greatest number of dynamic events occurs between these boundaries, under near and post-stall flow conditions.
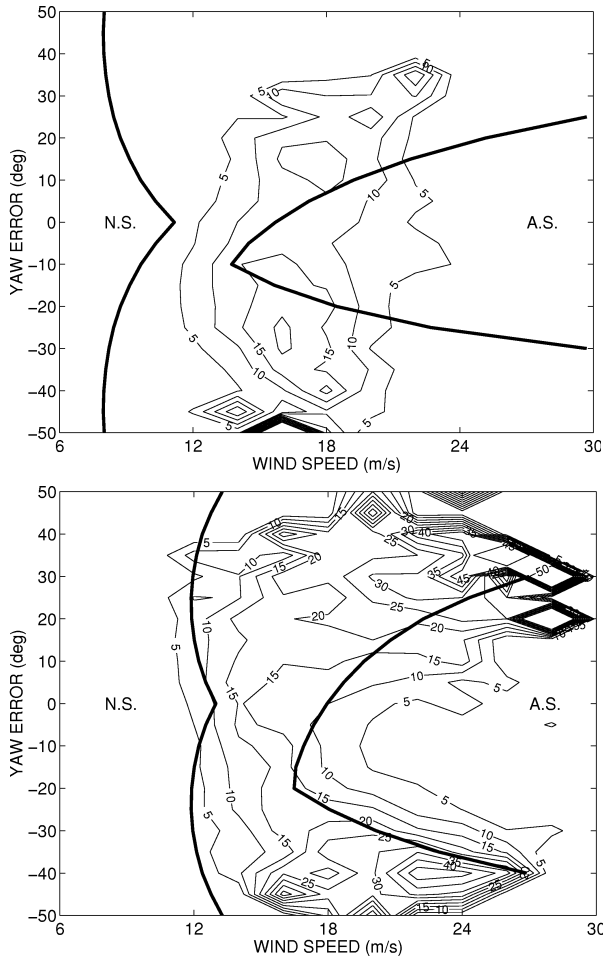
**Figure 8:** Percent of cycles where $C_p \leq -8.0$ (Phase IV).

locations, and flow remains separated over most of the operating velocities. Tower shadow tends to cycle these locations through stall much more often than with twisted blades. The increase in activity at 63% and 80% span locations for the untwisted and twisted blades, respectively, has not been resolved.
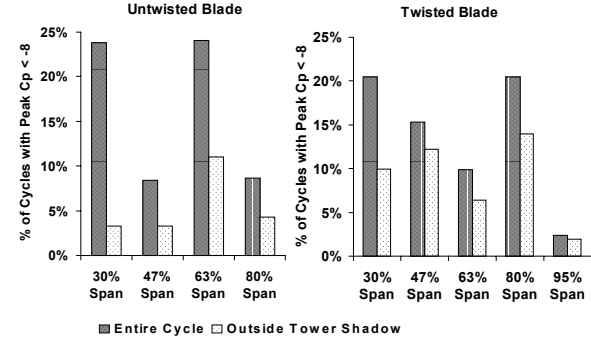


**Figure 9:** Tower shadow effects on dynamic loading.

Fig. 9 isolates tower shadow contribution to post-stall and unsteady aerodynamic events by showing counts of all cycles where $C_p \leq -8.0$ is reached (gray bars), and those cycles where $C_p \leq -8.0$ is reached outside tower shadow influence (speckled bars). The latter was accomplished by excluding any such events occurring at $150° \leq \phi \leq 240°$. Fig. 4 showed that cycle mean velocities are most numerous at lower velocities (~10 m/s) where flows tend to be attached and dynamic effects are _less_ prevalent. Thus, the average number of total cycles exhibiting dynamic effects is skewed _lower_ than would be expected under normal operating conditions.

In Fig. 9, the first substantial difference between the blade geometries is observed. The untwisted rectangular planform blade is much more sensitive to tower shadow effects than the twisted blade. Also, dynamic effects at 80% span are more prevalent for the twisted blade and cannot be attributed to tower shadow alone. This behavior will be shown to have a direct effect on the integrated blade bending moment ($C_M$). The untwisted blade has much higher $\alpha$ values at inboard span

Time series data showing the chordwise $C_p$ distribution through the rotation cycle highlight the complex aerodynamic response of the blades under different flow conditions. Both blades at zero yaw error and similar inflow velocities ($V_\infty = 8$ m/s) exhibit similar behaviors, but for different reasons. The untwisted blade is at $\alpha = 17°$ and the flow should be separated (Fig. 10a). Three-dimensional cross flow at this 30% span location produces a dynamic reattachment. Reattachment followed by a slight dynamic stall event occurs as the blade passes through the tower shadow ($150° \leq \phi \leq 240°$). In contrast, the twisted blade at the same wind speed had an angle of attack $\alpha = 4°$. The flow remained attached until the blade passed through the tower shadow, again producing separation and a slight dynamic stall event (Fig. 10b).

These effects are relatively benign when compared to the large changes introduced by yaw error (Fig. 11). In this figure, the two time series plots correspond to yaw errors of $\varphi = +20°$ and $-20°$ for the twisted blade at 80% span and $V_\infty = 20$ m/s. The $C_p$ variation can be correlated with the changes in $\alpha$ shown in Fig. 3. For positive yaw (Fig. 11a), $\alpha$ decreases with $\phi$ and reattaches prior to the tower shadow. Through the tower shadow, $\alpha$ and yaw error effects are additive, rapidly pitching the blade through stall. The pitch through a larger cumulative stall angle due to the yaw contribution more than likely exacerbates the peak pressure and transient load from the dynamic separation event. The flow remains separated throughout the remainder of the cycle. Behavior at $\varphi = -20°$ (Fig. 11b) is quite different. Here, a minimum $\alpha$ is achieved at $\phi = 0°$. This produces two reattachment points in the rotation cycle, $\phi = 0°$ and $\phi = 180°$ (tower shadow).

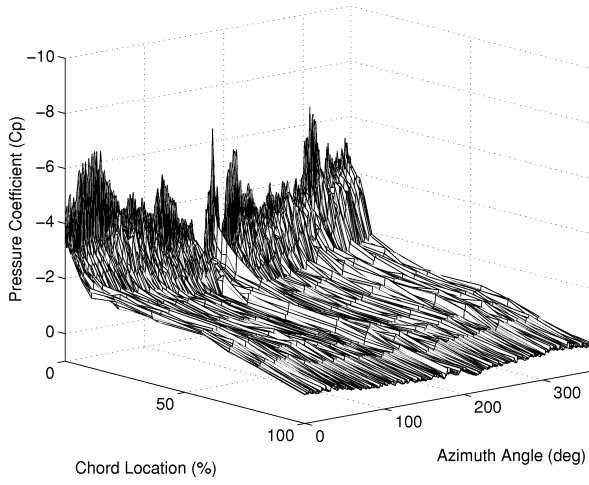**Figure 10(a):** Surface pressure distribution versus azimuth angle (Untwisted blade, $V_\infty$ = 8 m/s, $\varphi$ = 0°, 30% span).
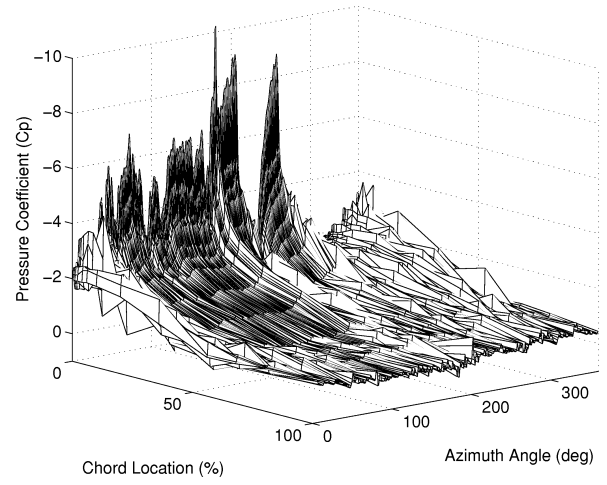


**Figure 11(a):** Surface pressure distribution versus azimuth angle (Twisted blade, $V_\infty$ = 20 m/s, $\varphi$ = 20°, 80% Span).
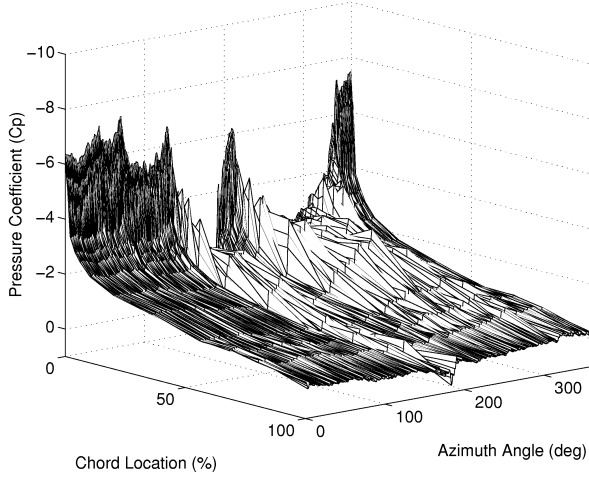


**Figure 10(b):** Surface pressure distribution versus azimuth angle (Twisted blade, $V_\infty$ = 8 m/s, $\varphi$ = 0°, 30% span).
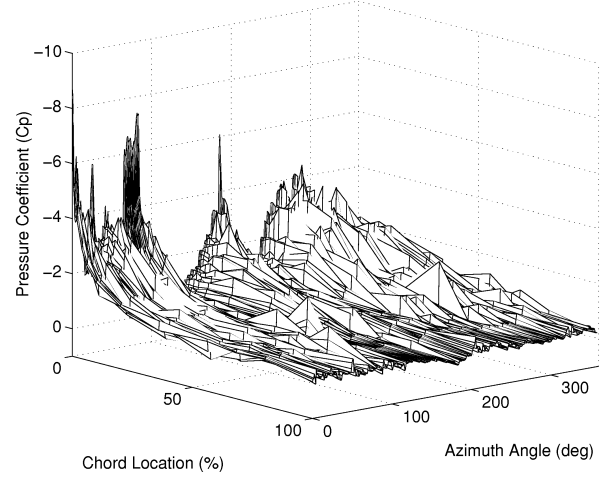


**Figure 11(b):** Surface pressure distribution versus azimuth angle (Twisted blade, $V_\infty$= 20 m/s, $\varphi$ = -20°, 80% Span).

Tower shadow creates another interesting performance anomaly in the near and post-stall regime. Depending on the inflow conditions and the local blade angle of attack, the interaction between the blade and tower shadow can create a bifurcation in the quasi-static pressure distribution. Passage through the tower shadow can prompt surface pressure distributions to transition from attached to separated, or from separated to attached. Alternatively, tower shadow passage can result in no significant change to the flow state, with either attached or separated conditions persisting before, during, and after tower shadow interaction. Significantly, although the perturbation elicited from the brief tower wake interaction itself may be small, the state change in quasi-static load when integrated over the rotation cycle is not. Several unsteady parameters including $V_\infty$, $\varphi$, unsteady wake hysteresis, and behavior of any three-dimensional stall can have an effect on the bifurcation response. Although difficult to quantify, this tower shadow effect occurs with sufficient frequency to warrant further investigation. The potential link between this bifurcated response and quasi-static stall hysteresis creating the observed state change should also be examined.
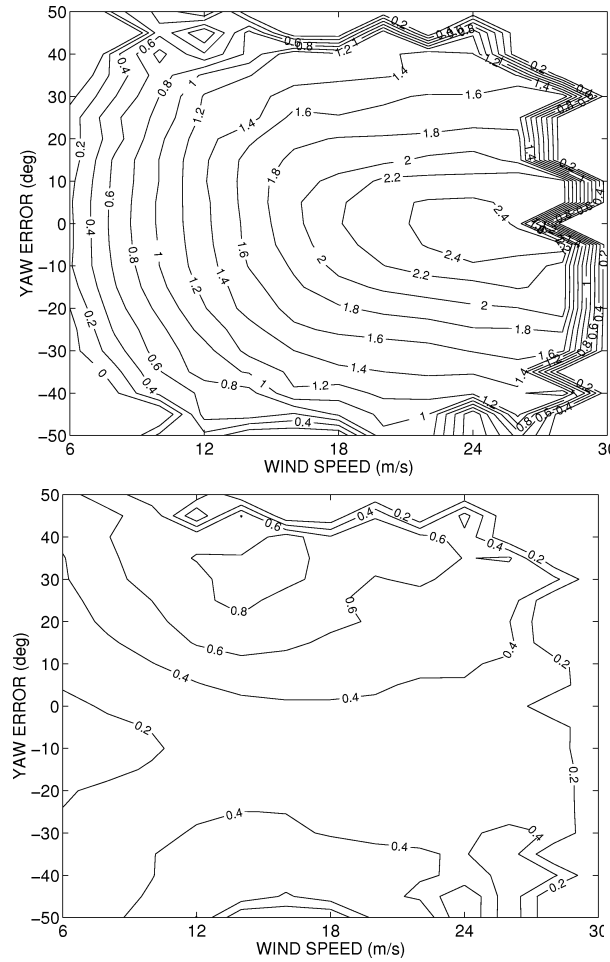
Variation in normal force coefficient ($C_N$) over the blade rotation cycle also was used to quantify each blade's three-dimensional dynamic response. In Figs. 12 and 13, $C_N$ was obtained from direct integration of the $C_p$ data for the 30% and 80% span locations respectively. Both cycle mean and standard deviation values for $C_N$ were binned on mean $V_\infty$ and $\varphi$. Responses for the twisted and untwisted blades were similar and only the twisted blade data are shown here. In Fig. 12, at higher wind speeds, average $C_N$ values exceed 2.4 at 30% span – over two times greater than static two-dimensional wind tunnel data predicts.
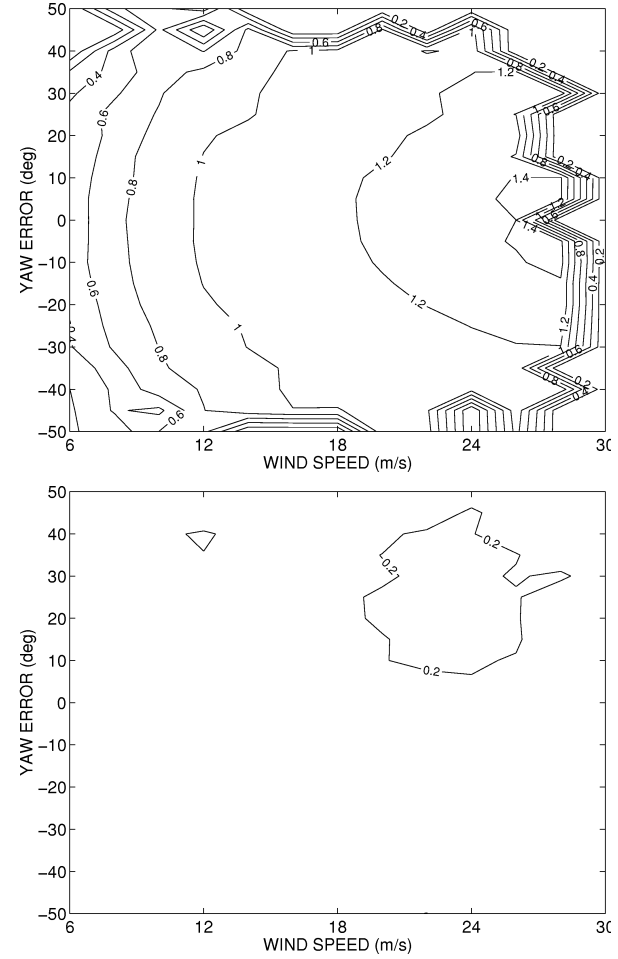


**Figure 13:** Average and standard deviation for $C_N$ for twisted blade at 80% span.

The standard deviation in $C_N$ is a direct measure of the dynamic load fluctuation during the cycle for a given $V_\infty$ and $\varphi$. At 30% span (Fig. 12), the lowest values occur along the $\varphi = 0°$ axis (zero yaw error). Significant dynamic effects are observed with increasing $\varphi$ where values of 1.0 are obtained at 30° $\varphi$. At this level, deviations in normal force produce average fluctuations on the same order of magnitude as the maximum $C_N$ values obtained from static wind tunnel tests. The effect is asymmetric with yaw. Larger deviations occur with positive



**Figure 12:** Average and standard deviation for $C_N$ for twisted blade at 30% span.

yaw error, where the tower shadow and yaw error effects on $\alpha$ are complementary in $\phi$.

At 80% span (Fig. 13), the changes in $C_N$ with $V_\infty$ and $\phi$ are less pronounced than those at 30% span. However, average $C_N$ values of 1.5 still far exceed quasi-static wind tunnel performance data. Deviation in normal force is also less prominent than for the 30% span location, but still of significant magnitude. As at 30%, the standard deviation distribution is asymmetrical with respect to yaw error, with the maximum occurring at 25° yaw error.

$C_N$ mean values respond differently for the two blade geometries. For the untwisted blade, the entire $C_N$ response centroid is shifted to higher wind speeds at increasing span locations (not shown). This effect appears to simply reflect the decrease in $\alpha$ with increasing span for any wind speed. Equivalent angles of attack are achieved with higher wind speeds. A strong similarity exists in both cycle averaged and dynamic response at incremental span locations of 47% and 63% (not shown) with peak magnitudes diminishing slightly ($\approx$10%) at 80% span. In contrast, $C_N$ mean values for the twisted blade do not shift. At low wind speeds, $C_N$ contours are quite similar across all span locations, reflecting the uniformity

in $\alpha_i$ at the designed wind speed. Increasing wind speed broadens the bands at any span location but does not shift the overall response curve. Again, this is consistent with the non-uniform increase in $\alpha$ with higher wind speeds over the span.

Dynamic activity, as measured by the $C_N$ standard deviation, decreases with increasing span for both geometries. However, twisted blade dynamic activity is much greater. Blade root $C_M$ data obtained from strain gage measurements are plotted as $C_M$ means and standard deviations for both the untwisted and twisted blade geometries (Figs. 14 and 15). Standard deviation of root flap bending is greatest at increased $V_\infty$ for both positive and negative values of $\phi$. This unsteady behavior correlates best with the high incidence of cycles where $C_p \leq -8.0$ in Fig. 8. Logically, the high percentage of cycles with large pressure fluctuations at 80% span will produce the greatest standard deviation in the root flap load. Interestingly, however, 80% span for the untwisted blade shows similar pressure cycle activity without the resulting $C_M$ behavior. Whether this effect reflects data density variance, variance due to quasi-static mean $C_N$ participation at various spans, or a true three-dimensional dynamic effect resulting from geometry or separation effects has not been resolved at this time.
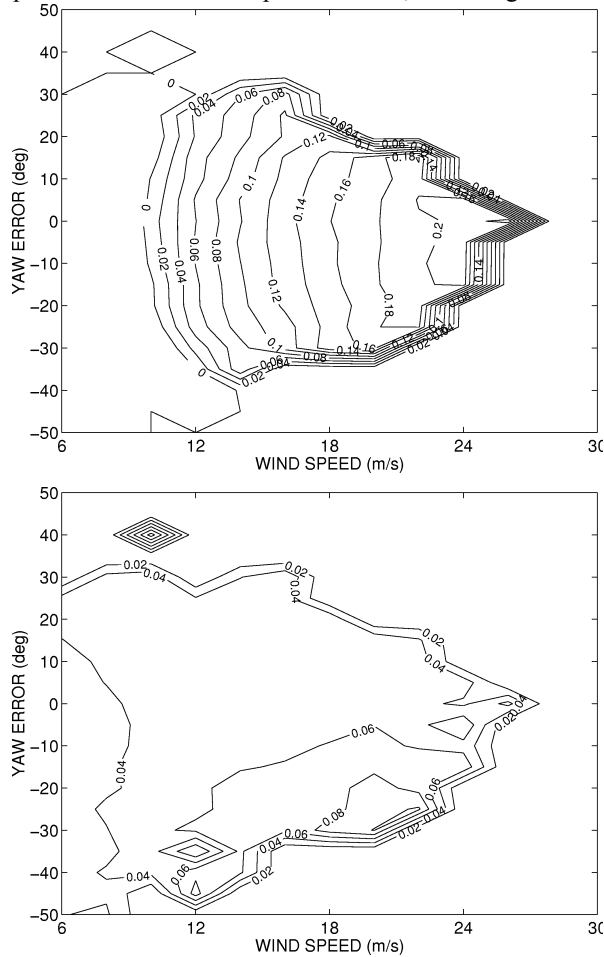


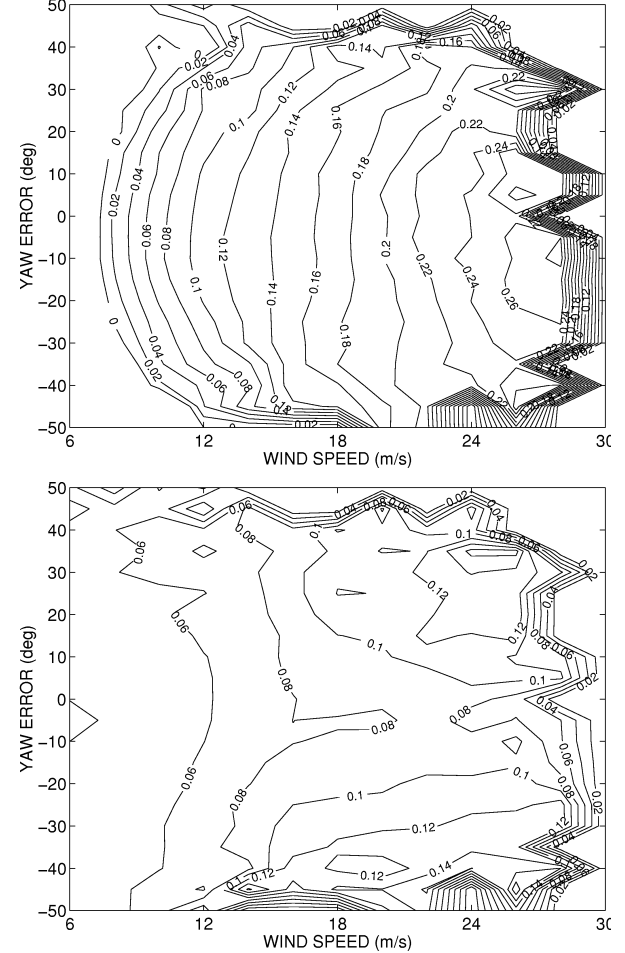**Figure 14:** Average and standard deviation for $C_M$ for untwisted blade.



**Figure 15:** Average and standard deviation for $C_M$ for twisted blade.

10

## CONCLUSIONS

Aerodynamic performance was compared for two rectangular planform wind turbine blades having S809 airfoil cross-sections. These blades differed only in three-dimensional geometry, with one blade being untwisted and the other having an optimized twist distribution. These comparisons were based on field test data acquired at the National Wind Technology Center. Both blades exhibited two-dimensional aerodynamic performance at inflow conditions where the local blade angle was below static stall.

Significant variations in performance were noted under near- and post-stall conditions. Peak pressure distributions and mean aerodynamic loads were far in excess of two-dimensional wind tunnel data. Individual pressure time series for select test cycles indicated both three-dimensional flow effects as well as dynamic stall contributed to these enhanced loads.

Both blades were more dynamically active under near- and post-stall operation. This effect increased with both mean velocity and yaw error. Certain combinations of $V_\infty$ and $\varphi$ exacerbated the effect and were correlated to cycles with high peak pressure coefficients at 80% span. The twisted blade was observed to be more dynamically active than the rectangular blade. It is not clear if this effect reflects data density variance, variance as a result of quasi-static mean $C_N$ participation at various spans, or a true three-dimensional dynamic effect resulting from geometry and/or separation behavior.

Influence of the tower shadow was observed to have a greater effect than expected. The rapid change in local blade angle produced the expected dynamic stall events. However, the same effect was also observed to "bifurcate" the steady state aerodynamic response introducing "state" changes between attached and separated flow over the cycle. The number of occurrences was significant enough in the random sampling of pressure time series selected to warrant further investigation.

This overview of key aerodynamic influences impacting wind turbine operation has highlighted some pressing problems and promising opportunities. The flow fields that most stubbornly resist comprehension and actively challenge design are three-dimensional, unsteady, and separated. Aerodynamics modeling strategies continue to advance, but cannot yet predict these types of flows with sufficient accuracy and reliability. Field experiments can successfully characterize these flow field effects. However, bounds on spatial and temporal resolution coupled with the impossibility of controlling inflow conditions limit the understanding thus gained.

Cause exists for optimism, however. Later this year, the NWTC Unsteady Aerodynamics Experiment is projected to enter the NASA Ames 80 ft x 120 ft wind tunnel. This series of experiments will enable full-scale wind turbine flow field measurements, and allow command of inflow and other parameters that defy control in the field. Exploitation of the data thus acquired will augment comprehension of three-dimensional unsteady separated flows elicited by wind turbines. In addition, these data will facilitate development of enhanced aerodynamic modeling strategies. Improved understanding of complex wind turbine aerodynamics formalized in accurate, robust models will constitute a powerful capability for analyzing and designing wind energy machines of the future.

## REFERENCES

[1] Schepers, J.G.; Brand, A.J.; Bruining, A.; Graham, J.M.R.; Hand, M.M.; Infield, D.G.; Madsen, H.A.; Paynter, R.J.H.; Simms, D.A. (1997), "Final Report of IEA Annex XIV: Field Rotor Aerodynamics," ECN-C-97-027, Petten, Netherlands.

[2] Butterfield, C.P.; Musial, W.P.; Simms, D.A. (1992). "Combined Experiment Phase I Final Report." NREL/TP-257-4655. Golden, CO: National Renewable Energy Laboratory.

[3] Huyer, S.A.; Simms, D.A.; Robinson, M.C. "Unsteady Aerodynamics Associated with a Horizontal-Axis Wind Turbine." American Institute of Aeronautics and Astronautics Journal, Volume 34, No. 10, pp. 1410-1419, 1996.

[4] Miller, M.S.; Shipley, D.E.; Young, T.S.; Robinson, M.C.; Luttges, M.W.; Simms, D.A. (1995), "The Baseline Data Sets for Phase II of the Combined Experiment." NREL/TP 442-6915, Golden, CO: National Renewable Energy Laboratory.

[5] Miller, M.S.; Shipley, D.E.; Young, T.S.; Robinson, M.C.; Luttges, M.W.; Simms, D.A. (1995), "Combined Experiment Phase II Data Characterization." NREL/TP 442-6916, Golden, CO: National Renewable Energy Laboratory.

[6] Robinson, M.C.; Simms, D.A.; Hand, M.M.; Schreck, S.J. "Vortex/Blade Interaction from Tower Shadow Effects." In preparation.

[7] Carr, L.W.; "Progress in Analysis and Prediction of Dynamic Stall." American Institute of Aeronautics and Astronautics Journal, Volume 25, No. 1, pp. 6-17, 1988.

[8] McCroskey, W.J. "Some Current Research in Unsteady Fluid Dynamics-The 1976 Freeman Scholar Lecture." Transactions of the ASME Journal of Fluids Engineering. March, 1977.

[9] Somers, D.M. (1997), "Design and Experimental Results for the S809 Airfoil," NREL/SR 440-6918, Golden, CO: National Renewable Energy Laboratory.